Neural Networks 22 (2009) 1257–1270

Contents lists available at ScienceDirect

Neural Networks

journal homepage: www.elsevier.com/locate/neunet

2009 Special Issue

Mapping broadband electrocorticographic recordings to two-dimensional hand trajectories in humans
Motor control features

Aysegul Gunduz [a,*], Justin C. Sanchez [b], Paul R. Carney [b], Jose C. Principe [a]

[a] Computational NeuroEngineering Laboratory, Department of Electrical and Computer Engineering, United States
[b] Department of Pediatrics, Division of Neurology University of Florida, Gainesville, FL 32611, United States

ARTICLE INFO

Article history:
Received 30 September 2008
Received in revised form 25 June 2009
Accepted 27 June 2009

Keywords:
Brain–machine interfaces
Human neuroprosthesis
Electrocorticography
Motor control
Neural decoding

ABSTRACT

Brain–machine interfaces (BMIs) aim to translate the motor intent of locked-in patients into neuroprosthetic control commands. Electrocorticographical (ECoG) signals provide promising neural inputs to BMIs as shown in recent studies. In this paper, we utilize a broadband spectrum above the fast gamma ranges and systematically study the role of spectral resolution, in which the broadband is partitioned, on the reconstruction of the patients' hand trajectories. Traditionally, the power of ECoG rhythms (<200–300 Hz) has been computed in short duration bins and instantaneously and linearly mapped to cursor trajectories. Neither time embedding, nor nonlinear mappings have been previously implemented in ECoG neuroprosthesis. Herein, mapping of neural modulations to goal-oriented motor behavior is achieved via linear adaptive filters with embedded memory depths and as a novelty through echo state networks (ESNs), which provide nonlinear mappings without compromising training complexity or increasing the number of model parameters, with up to 85% correlation. Reconstructed hand trajectories are analyzed through spatial, spectral and temporal sensitivities. The superiority of nonlinear mappings in the cases of low spectral resolution and abundance of interictal activity is discussed.

1. Introduction

Collected through subdural electrode grids, ECoG signals are the cumulative sum of dendritic activity and postsynaptic potentials from synchronized sources with finer spatial resolution and higher signal-to-noise ratios compared to EEG recordings (Leuthardt, Schalk, Moran, & Ojemann, 2006). Most importantly, ECoG signals yield much broader spectra since the electrode grids are below the skull and scalp media which act as lowpass filters in EEG recording techniques (Nunez & Srinivasan, 2005). However, this advantage of ECoG over EEG has not been exploited in previous ECoG BMI studies as the clinical recording systems employed were designed for the collection of EEG at low sampling rates (<1 kHz). Unlike the implantation of intracortical microelectrode arrays, which are restricted to limited cases in human subjects (Donoghue, Nurmikko, Black, & Hochberg, 2007; Hochberg et al., 2006; Kennedy, Kirby, Moore, King, & Mallory, 2004), ECoG has been used extensively in the localization and resection of epileptogenic focus of humans for decades (Leuthardt et al., 2006).

Electrocorticography (ECoG) provides an intermediate level of brain activity between intracortical and scalp (EEG) recordings, and its potential as a BMI input signal has been demonstrated through hand movement classification (Chin et al., 2007), hand direction classification (Mehring et al., 2004), and one-dimensional hand trajectory prediction (Felton, Wilson, Williams, & Garell, 2007; Leuthardt, Schalk, Wolpaw, Ojemann, & Moran, 2004). ECoG BMIs that decode two-dimensional hand trajectories have not emerged until recently due to the many clinical and signal processing (feature extraction and translation) challenges involved. ECoG is the spatiotemporal smoothed sum of dendritic activity from millions of neurons over a pial surface of 1–1.5 cm^2 (Freeman, 2006) and thus many of the feature extraction issues arise from the fact that motor encoding with ECoG is not as straightforward as firing rates of single unit activities.

Since ECoG signals represent a diverse set of cortical rhythms, spectral analysis is typically the first level method used to derive control signals for a neuroprosthesis. For the reconstruction of movement trajectories there are still many unknown aspects

* Corresponding address: Computational NeuroEngineering Laboratory, Department of Electrical and Computer Engineering, P.O. Box 116130, Building #33, Center Drive, Room NEB 486, Gainesville, FL, 32611, United States. Tel.: +1 352 392 2682; fax: +1 352 392 0044.
E-mail addresses: aysegul@cnel.ufl.edu (A. Gunduz), jcs77@ufl.edu (J.C. Sanchez), carnepr@peds.ufl.edu (P.R. Carney), principe@cnel.ufl.edu (J.C. Principe).

0893-6080/$ – see front matter © 2009 Elsevier Ltd. All rights reserved.
doi:10.1016/j.neunet.2009.06.036

of which bands in the available ECoG spectrum are the most relevant for control. Schalk et al. (2007) studied movement-related spectral changes in seven frequency bands from 8 Hz to 190 Hz, and amplitude changes in moving averages in raw ECoG in 333 ms windows (yielding a total of 8 features per 64 channels) and mapped linearly to two-dimensional trajectories with no further memory depth. The correlation coefficients between the kinematics and the model outputs for in five cross-validation folds were between [0.50, 0.81] (with a median of 0.71) and [0.18, 0.80] (with a median of median 0.51) for the subject with the highest performance. The sensitive areas were found to be the motor and pre-motor cortices (Brodmann areas 4 and 6). Pistohl, Ball, Schulze-Bonhage, Aertsen, and Mehring (2008) lowpass filtered ECoG signals which were already recorded at low sampling rates of 256 Hz or 1024 Hz with 0.75 s windows of Savitsky–Golay filters. The smoothed signals from all channels formed the measurement vector at time $(t - \tau)$ and the hand kinematics at time t formed the state vector to be used in a Kalman filter (the optimal value of τ was found empirically to be 125 ms). Across all trials correlation coefficients of 0.40 ± 0.1 were attained with two patients that had coverage over the motor area. In neither of these two-dimensional studies is the broadband characteristics of ECoG utilized beyond the fast gamma range, nor have nonlinear translation functions have been employed. Moreover, time embedding is only facilitated by the window sizes in which the feature vectors are computed. However, in animal studies memory depths up to 1 s into the past have been utilized (Carmena et al., 2003; Wessberg et al., 2000).

In previous studies, we had utilized the broader spectra of ECoG over EEG and shown presence of motor features in ECoG recordings from patients tracing two-dimensional trajectories up to 6 kHz through reconstructed trajectories in coarse spectral ranges (1–60 Hz, 60–100 Hz, 100–300 Hz, 300 Hz–6 kHz) (Gunduz, Ozturk, Sanchez, & Principe, 2007; Sanchez, Gunduz, Carney, & Principe, 2008), as well as in exploratory studies with finer spectral decomposition (Gunduz, Sanchez, Carney, & Principe, in preparation). The results of these studies indicated that there is a sophisticated performance relationship between the total spectral bandwidth, resolution of spectral decomposition used for extracting control features, and the choice of decoding model (linear or nonlinear) for translating features into control commands. For BMIs high-dimensional multiple-input–multiple-output (MIMO) systems are common and one must balance the number of model parameters and the optimization of the projection from neural activity to behavior. Utilizing broad spectra and embedding more time samples undoubtedly increases the number of model parameters. In this paper, we empirically investigate the optimal ECoG spectral ranges and spectral resolution (number of spectral bands and their bandwidths) and translation topologies for reconstructing two-dimensional hand trajectories. Our overall goal is to find modulations in the minimal configuration of spectral bands, memory depths on the feature extraction end and the simplest model architectures that could be implemented for real-time applications.

Optimal spectral resolution in the broad spectrum and optimal memory depths are found empirically by adaptive linear models such as Wiener filters (Haykin, 2001), normalized least mean squares (Haykin, 2001) and gamma filters (Principe, Vries, & Oliveira, 1993) with tap delay lines (TDLs). These three types of linear filter provide a simple analytic solution, online feasibility while compensating for system nonstationarities and decreased number of model parameters without compromising memory depth, respectively. Although linear filters have well established, in low-complexity training methodologies, the reconstructed trajectories may be suboptimal since the output is limited to mappings in the input space and the intrinsic neurophysiological mapping of control features to motor behavior may involve nonlinear translations (Gunduz et al., 2007). Again in our preliminary studies with low spectral resolution, we reported higher performance results in reconstruction of two-dimensional trajectories with nonlinear projections (Gunduz et al., 2007). Therefore, herein, we also study modeling hand movements from spectral ECoG features using artificial neural networks, specifically echo state networks (ESNs) (Jaeger, 2001) and leaky echo state networks (Rao et al., 2005). These neural networks were chosen over time-delay neural networks (TDNNs) due to the reduced number of parameters by embedding memory through recurrencies. Moreover, ESNs have training complexities equivalent to Wiener filters which do not require backpropagation through time. Performance of the linear and nonlinear filters are compared based on reconstruction metrics, spectral resolution and presence of interictal artifacts.

Table 1
Motor response to electrical stimulation of subdural grids.

Patient 1		Patient 2	
Right hand	22, 28	Right hand	2,3
Right wrist	23, 24, 30	Right arm	14, 15
Right forearm	22, 30		
Right bicep	29		
Right sensory arm	27		

2. Materials

The subjects volunteering in the behavioral experiments were being monitored for the treatment of intractable complex partial epilepsy at Shands Hospital at the University of Florida. Patient 1 was implanted with a 6×6 subdural grid and Patient 2 was implanted with a 4×8 grid, both over left fronto-temporal regions covering the PMd, M1, PP motor cortices. The grids consisted of a 1.5 mm thick silastic sheet embedded with platinum-iridium electrodes of 4 mm diameter, 2.3 mm diameter exposed surface and 1 cm center-to-center distances. Electrical stimulation of the subdural grids (Uematsu et al., 1992) further guided the localization of the primary motor cortex (for further details see Sanchez et al. (2008)). Motor responses from the stimulation, using the enumeration convention in Fig. 1 are provided in Table 1. Both patients executed the tasks with their right hands. The experimental paradigms were approved by the University of Florida Institutional Review Board.[1]

For our behavioral experiments, a separate 32 channel system[2] capable of recording ECoG at a sampling rate of 12 kHz and 16 bits of resolution was set up due to the limited bandwidth of the system available in the clinic for epilepsy monitoring. The desired behavioral trajectories were generated by a desktop computer running Matlab v7 which communicated with a bank of DSPs (Tucker–Davis Pentusa base-station) processing the amplified ECoG signals. The desired trajectories were sent to a second computer monitor placed in front of the patients. Behavioral trajectory recordings were also stored with a shared time clock on the Pentusa system. (For further details on the signal acquisition system please refer to Gunduz et al. (in preparation).)

Patients were asked to trace a predefined cursor trajectory presented on an LCD screen with an active area of 20×30 cm with their right index finger. Snapshots of the screen as observed by the patients during experimentation are presented in Fig. 2. The paradigm consists of a center-out cursor control task (Georgopoulus, Kalaska, Caminiti, & Massey, 1982) and a

[1] http://irb.ufl.edu/.

[2] Activity from electrodes 33–36 of the implanted 6×6 grids of Patient 1 were not recorded.

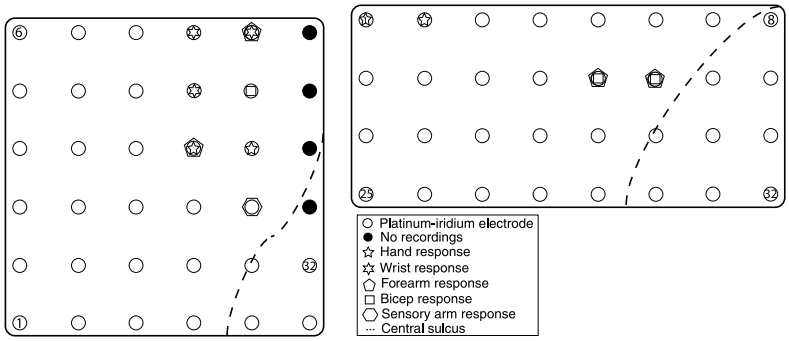

Fig. 1. Motor responses to electrical stimulation superimposed on the subdural electrode grids implanted in Patient 1 (on the left) and Patient 2 (on the right) with the central sulcus as reference.

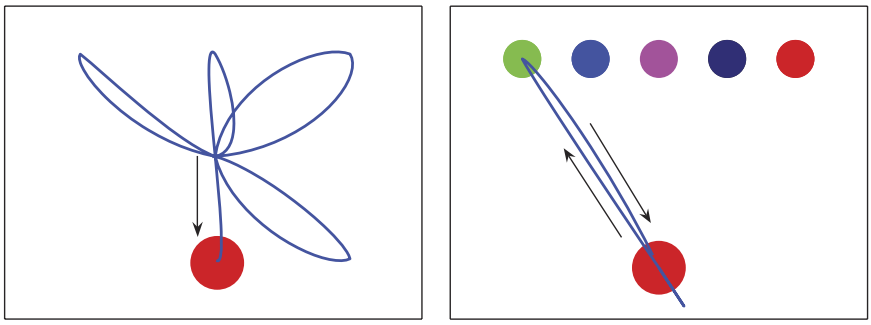

Fig. 2. Behavioral trajectories on a 20 × 30 cm screen. Center-out trajectory is shown on the left and the target selection task is shown on the right.

Table 2
ECoG spectral frequency bands.

Spectral bands with $n = 32$ (Hz)	$n = 16$ (Hz)	$n = 8$ (Hz)
8–10	8–12	8–18
10–12		
12–15	12–18	
15–18		
18–23	18–28	18–42
23–28		
28–34	28–42	
34–42		
42–52	42–63	42–96
52–63		
63–88	63–106	
88–96		
96–118	96–145	96–219
118–145		
145–178	145–219	
178–219		
219–270	219–331	219–501
270–331		
331–408	331–501	
408–501		
501–616	501–758	501–1147
616–758		
758–932	758–1147	
932–1147		
1147–1410	1147–1734	1147–2623
1410–1734		
1734–2133	1734–2623	
2133–2623		
2623–3226	2623–3967	2623–6110
3226–3967		
3967–4879	3967–6110	
4879–6110		

target selection task (Desmurget, Pelisson, Rossetti, & Prablanc, 1998) repeated consecutively five times. These behaviors mimic a computer user's selection of an icon on the screen. All behavioral tasks were acquired concurrently with the ECoG activity and further downsampled to 10 Hz.

3. Methods

For a systematic analysis, the broadband spectrum is decomposed into non-overlapping intervals of equal bandwidth in the logarithmic frequency domain through a bank of *constant-Q filters* which yield narrow bandwidths for slower central frequencies and wider passbands for faster central frequencies, mimicking natural brain rhythms. The time-frequency domain properties of constant-Q filters, for example, yield a reasonable model for cochlear preprocessing (Smaragdis, 2001). The logarithmic spectral range from 8 Hz to 6 kHz is uniformly divided into $n = 32, 16, 8$ bands as shown in Table 2 for empirical spectral resolution analysis (see Gunduz et al. (in preparation) for details on the selection of the number of passbands and Q-filter parameters). The modulation of ECoG components related to movement can be captured by the power of bandpass filtered ECoG signals computed in non-overlapping 100 ms time bins as follows:

$$x_j^k(t_n) = \int_{t_n}^{t_{n+1}} V_{j,k}^2(t)\mathrm{d}t \tag{1}$$

where $V_{j,k}$ is the filtered ECoG amplitude signal in frequency band k on channel j, and $t_{n+1} = t_n + 100$ ms. The ECoG features are labeled as $x_j^k(t)$, where $j = 1, 2, \ldots, 32$ indicates the electrode number as given in Fig. 1. For a systematic study of these features through event-related spectral, crosscorrelation, tuning and source separation analyses, please refer to Gunduz et al. (in preparation).

In the following subsections we describe in detail how the linear and nonlinear filters were implemented as well as the why these filters were chosen in particular. Sensitivity analysis, or the contribution of the spatial and spectral features, are provided and discussed for all filters along with the performance results. The improved performance is tested by taking the Wiener filter with the fewest number of spectral bands and memory depth resolution as a basis.

3.1. Linear mapping

We design linear models to map the extracted features from ECoG recordings to the position of the cursor on the screen which the patients are tracing with their right index fingers. The desired signals, donated by $d_X(t)$ and $d_Y(t)$, are the horizontal (x-axis) and vertical (y-axis) positions of the cursor (and thus the position of the right index finger of the patient) on the 20×30 cm display with the origin of the coordinate system at the center of the screen. Finally, the model outputs are given by $y_X(t)$ and $y_Y(t)$.

With adaptive linear filters the hand/cursor position at any given time is modeled through a function of the short-term history of the ECoG signal. Such a dynamical model requires a system with sufficient memory for a proper functional mapping from the neural modulations to the motor output. With the addition of tap delay lines (TDLs) at each channel, the number of filter parameters (the size of the weight matrix) becomes the product of the number of channels, $M = 32$, the number of output dimensions, $C = 2$, and the memory depth of the TDL, L, which is determined empirically. The TDL outputs are translated into the cursor coordinate system by means of the weight matrix, $\mathbf{w}$, and linear combiners. This operation is mathematically described below:

$$y_c(t) = \sum_{k=1}^{n} \sum_{i=0}^{L-1} \sum_{j=1}^{M} x_j^k(t-i)\mathbf{w}_c^k(i,j) + b_c^k \tag{2}$$

where c denotes one of the two output dimensions (horizontal, X- or vertical, Y-), $\mathbf{w}_c^k(i,j)$ is the (i,j)th entry of the weight matrix mapping activity in the kth band to the cth dimension and b_c^k is the estimation bias of the model which can be dropped if the inputs and desired signal are centered around their mean (Kim et al., 2006).

First, we employ a *Wiener filter with ridge regression* (Kim, 2005). The Wiener–Hopf equation (Haykin, 2001) is the analytical solution for minimization of the mean-squared error:

$$\mathbf{w}_c = (\mathbf{R} + \delta\mathbf{I})^{-1} \cdot \mathbf{P}_c \tag{3}$$

where $\mathbf{P}_c$ is the $L \times 1$ crosscorrelation vector between the ECoG activity and the trajectory in the cth dimension and $\mathbf{R}$ is the autocorrelation matrix of all ECoG activity, composed of $L \times L$ correlation matrices between each feature (channel power in a certain band) with the autocorrelation matrices of the individual features aligned at the diagonal in blocks and is not necessarily symmetric. Hence, with inadequate data lengths or noisy data, $\mathbf{R}$ may be estimated poorly and be close to singular with very high condition numbers (highly correlated input channels may especially cause the weight matrix to have an artificially large variance). δ is the ridge regression regularization term which conditions the inverse and is equivalent to solving a constrained least squares, i.e. minimizing the MSE with the constraint: $\|\mathbf{w}\|^2 \leq \rho$. Practically, δ is selected by a desirable value for the input signal-to-noise ratio (SNR) estimated by:

$$\text{SNR} \approx \frac{tr[\mathbf{R}]}{\delta}. \tag{4}$$

We set the desired SNR to 30 dB and empirically compute the trace of the covariance matrix and determine δ (Kim, 2005).

The Wiener filter provides the optimal analytic solution for stationary systems, however, the brain is a nonstationary dynamic system that generates different neural responses to the same stimulus. *Normalized least mean squares* (NLMS) is an online gradient descent algorithm which minimizes the instantaneous squared error, $\mathbf{e}^2(n)$, at a rate normalized by the power in the input

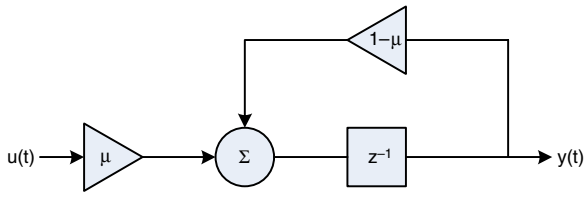

Fig. 3. The leaky integrator.

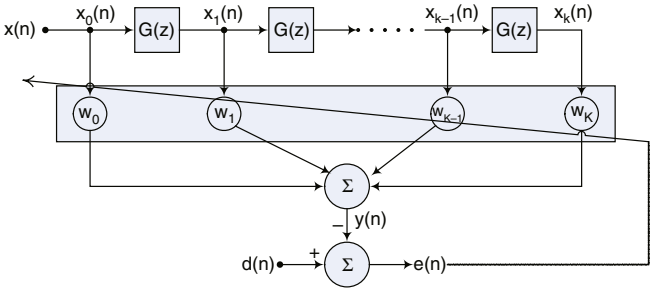

Fig. 4. Block diagram representation of a general linear filter. The gamma filter is implemented by substituting the leaky integrator in the transfer functions, $G(z)$. Note that $G(z) = z^{-1}$ reduces the structure to a tap-delay-line.

tap vector in order to contend with this problem (Haykin, 2001). The weight updates are formalized as:

$$\mathbf{w}(n+1) = \mathbf{w}(n) + \frac{\eta}{\sum_{j=1}^{M} \left\|\mathbf{x}_j(n)\right\|^2 + \gamma}\mathbf{e}(n)\mathbf{x}(n) \tag{5}$$

where $\mathbf{x}_j(n) = \begin{bmatrix} x_j(n) & x_j(n-1) & \cdots & x_j(n-L+1) \end{bmatrix}$ is the input tap vector at channel j and η is the learning rate or step size which adjusts the speed of convergence of the algorithm. γ is a small constant which prevents divergence in case of very small input signals.

As in the case with Wiener filters, the NLMS weights can have high variance due to correlated input channels. NLMS with *weight decay* aims to lower weight variance by placing an upper bound on the sum of weight magnitudes. The gradient descent update equation for the weights then becomes:

$$\mathbf{w}(n+1) = \mathbf{w}(n) + \frac{\eta}{\sum_{j=1}^{M} \left\|\mathbf{x}_j(n)\right\|^2 + \gamma}\mathbf{e}(n)\mathbf{x}(n) - \delta\mathbf{w}(n). \tag{6}$$

All three models thus far, are finite impulse response filters and their memory depths are coupled to the filter orders. For example, for L taps, M channels, n bands, and C output dimensions would require $L \times M \times n \times C$ parameters. The final linear filter we adopt is the *gamma filter* which decouples memory depth from filter order with restricted feedback (Principe et al., 1993). In other words, equal memory depths can be achieved with fewer model weights through leaky integrators depicted in Fig. 3 with the following transfer function:

$$G(z) = \frac{\mu}{z - (1-\mu)} \tag{7}$$

where $(1-\mu)$ is the gain in the feedback loop. The memory depth of a gamma filter is $D_K = \frac{K}{\mu}$ (i.e. can be adjusted by varying μ). The system equations for the variable shown in 4 are as follows:

$$Y(z) = \sum_{k=0}^{K} \mathbf{w}_k X_k(z) \tag{8}$$
$$X_k(z) = G(z)X_{k-1}(z), \quad k = 1, 2, \ldots, K$$
$$X_0(z) = X(z), \quad k = 1, 2, \ldots, K$$

Table 3
Filter performance comparisons for Patient 1.

n	Filter	L	# of param.	r_X	r_Y	MSE_X	MSE_Y
32	Wiener	8	8192	0.49 ± 0.15	0.86 ± 0.11	0.94 ± 0.64	0.36 ± 0.18
	NLMS	14	14336 (+1)	0.55 ± 0.21	0.87 ± 0.17	0.83 ± 0.50	0.34 ± 0.20
	Weight decay	14	14336 (+3)	0.45 ± 0.19	0.87 ± 0.14	0.85 ± 0.56	0.36 ± 0.15
	Gamma	8	8192 (+1)	0.33 ± 0.29	0.81 ± 0.22	0.82 ± 0.46	0.31 ± 0.16
16	Wiener	14	7168	0.55 ± 0.21	0.87 ± 0.17	0.83 ± 0.50	0.34 ± 0.20
	NLMS	25	12800 (+1)	0.64 ± 0.19	0.82 ± 0.25	0.81 ± 0.43	0.34 ± 0.24
	Weight decay	25	12800 (+3)	0.63 ± 0.21	0.80 ± 0.29	0.87 ± 0.59	0.36 ± 0.23
	Gamma	8	4096 (+1)	0.37 ± 0.31	0.81 ± 0.23	0.82 ± 0.38	0.34 ± 0.18
8	**Wiener**	**8**	**2048**	$\mathbf{0.52 \pm 0.25}$	$\mathbf{0.87 \pm 0.18}$	$\mathbf{0.84 \pm 0.58}$	$\mathbf{0.36 \pm 0.23}$
	NLMS	8	2048 (+1)	0.52 ± 0.25	0.86 ± 0.18	0.86 ± 0.59	0.35 ± 0.26
	Weight decay	8	2048 (+3)	0.44 ± 0.23	0.87 ± 0.21	0.90 ± 0.64	0.39 ± 0.22
	Gamma	8	2048 (+1)	0.37 ± 0.22	0.80 ± 0.27	0.84 ± 0.47	0.35 ± 0.23

Table 4
Filter performance comparisons for Patient 2.

n	Filter	L	# of param.	r_X	r_Y	MSE_X	MSE_Y
32	Wiener	8	8192	0.40 ± 0.21	0.65 ± 0.21	1.09 ± 1.12	0.67 ± 0.27
	NLMS	14	14336 (+1)	0.52 ± 0.20	0.77 ± 0.16	1.07 ± 0.94	0.63 ± 0.30
	Weight decay	14	14336 (+3)	0.53 ± 0.21	0.77 ± 0.16	1.05 ± 0.95	0.66 ± 0.29
	Gamma	8	8192 (+1)	0.54 ± 0.31	0.76 ± 0.25	1.15 ± 1.27	0.59 ± 0.22
16	Wiener	14	7168	0.47 ± 0.22	0.78 ± 0.15	1.08 ± 0.99	0.64 ± 0.26
	NLMS	14	7168 (+1)	0.51 ± 0.22	0.77 ± 0.16	1.07 ± 0.92	0.58 ± 0.26
	Weight decay	14	7168(+3)	0.58 ± 0.23	0.77 ± 0.19	1.01 ± 0.95	0.67 ± 0.26
	Gamma	8	4096 (+1)	0.54 ± 0.31	0.76 ± 0.25	1.15 ± 1.27	0.59 ± 0.22
8	**Wiener**	**8**	2048	$\mathbf{0.56} \pm 0.21$	$\mathbf{0.76} \pm 0.28$	0.98 ± 1.01	0.65 ± 0.22
	NLMS	25	6400 (+1)	0.52 ± 0.22	0.71 ± 0.24	0.99 ± 0.93	0.63 ± 0.23
	Weight decay	25	6400 (+3)	0.53 ± 0.22	0.71 ± 0.23	0.98 ± 0.98	0.59 ± 0.26
	Gamma	8	2048 (+1)	0.59 ± 0.27	0.72 ± 0.26	0.95 ± 1.16	0.55 ± 0.24

which yield the following system transfer function:

$$H(z) = \frac{Y(z)}{X(z)} = \sum_{k=0}^{K} \mathbf{w}_k \left(G(z)\right)^k. \tag{9}$$

The system is stable when the pole lies inside the unit circle, i.e. for $0 < \mu < 2$. For $\mu = 1$ the system reduces to a tap delay line. For $\mu < 1$ additional memory depth is supplied for low frequency components at the expense of the high frequency components. This would be desirable in our filter design as the hand trajectories oscillate at low frequencies (refer to Gunduz et al. (in preparation)).

3.1.1. Comparison of linear filters

Patient 1 performed five trials of center-out task followed by target selection in 3.87 min from which the first three trials is used for training and the remaining trials are used for testing the models. Patient 2 performed four trials in 4.65 min of which the first 3.5 min were used in model training. The performance of the models are quantified in each dimension (horizontal and vertical) by Pearson's r which indicates the degree of linear dependence between the reconstructed and the actual hand trajectories, and by the normalized mean squared error (MSE). Both of the above measures are computed over non-overlapping windows of 20 s and the mean and standard deviations of these measures on the test set are reported as the performance statistics.

Over four choices of linear filters, three choices of spectral resolution and memory depths varying from 800 ms to 2.5 s, t-tests with comparison to the lowest order Wiener filter[3] did not statistically identify the best combination, i.e. the performances were found to be statistically equivalent, attributable to high standard deviations in the performance metrics. For each filter the performance results with the best mean value and lowest standard deviation are reported in Tables 3 and 4. The output trajectories of the Wiener filters in Tables 3 and 4 are plotted in Figs. 5 and 6, for Patients 1 and 2, respectively.

3.1.2. Sensitivity analysis

Given the wide spectrum of ECoG used in these studies and the fine resolution of the decomposition, we seek to determine the ranking of the important electrode locations and spectral bands in terms of their contribution to behavior. To quantify the most important control signals, a sensitivity analysis was performed (Sanchez, Carmena, Lebedev, Nicolelis, & Harris, 2003). The magnitude of weights corresponding to channels and spectral bands can be used as a sensitivity measure since the outputs are directly related to the input taps through the weight function if the modeling error is sufficiently small and is mathematically defined as:

$$S_j^k = \frac{1}{2L} \sum_{c=X,Y} \sum_{i=0}^{L-1} |\mathbf{w}_c^k(i,j)|. \tag{10}$$

We further average the sensitivities across frequency bands (over k) to attain spatial sensitivity and across electrode grids (over j) to attain spectral sensitivity. These measures are presented in Figs. 7 and 8 for Patients 1 and 2, respectively. The spatial sensitivity of the $n = 32$ bands is widespread with high localizations in the PMd and M1 areas. Three of Patient 1's M1 electrodes for which hand, wrist, forearm and bicep responses to electrical stimulation were observed are revealed to have high sensitivities. With Patient 2, the M1 electrode for which a hand response was observed is identified as sensitive.

3.2. Nonlinear mapping

ECoG is the sum of dendritic activity of many sources propagated to the subdural surface, those modulating the motor

[3] A Wiener filter of order $L = 8$ in $n = 8$ spectral bands is the simplest linear filter design.

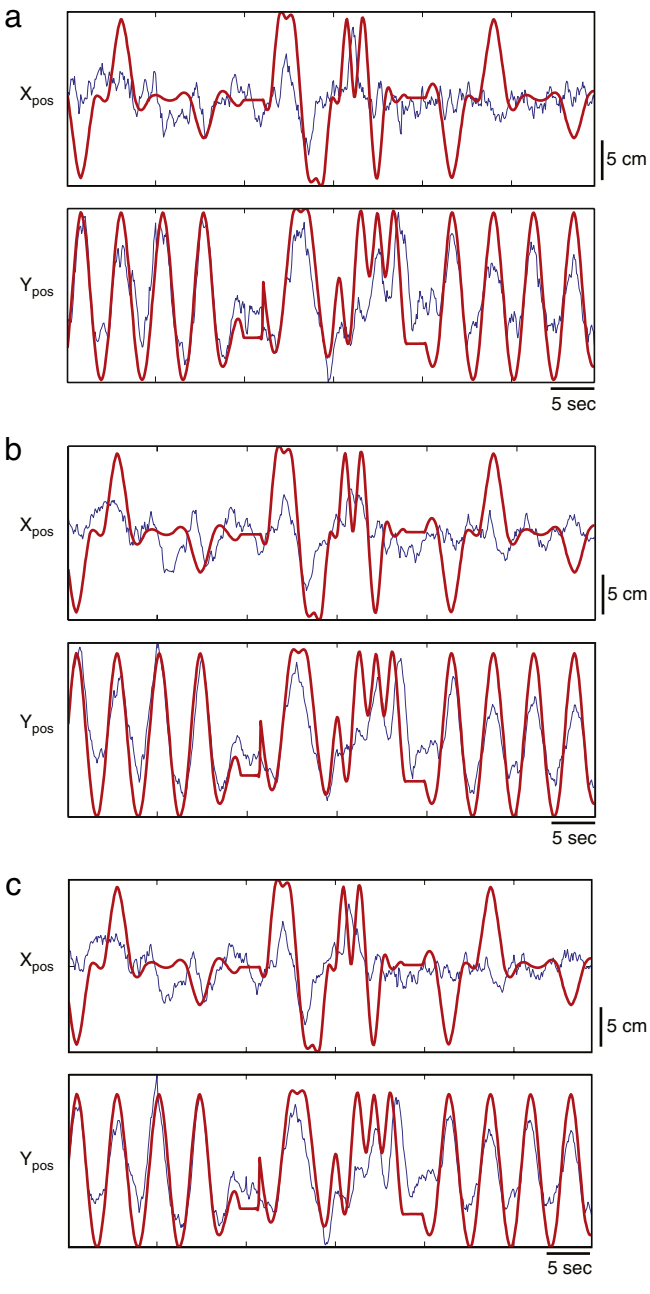

Fig. 5. Reconstructed trajectories from Wiener filters for Patient 1 (in blue) projected on the cursor trajectories (in red) with (a) $n = 32$, (b) $n = 16$, (c) $n = 8$ bands. (For interpretation of the references to colour in this figure legend, the reader is referred to the web version of this article.)

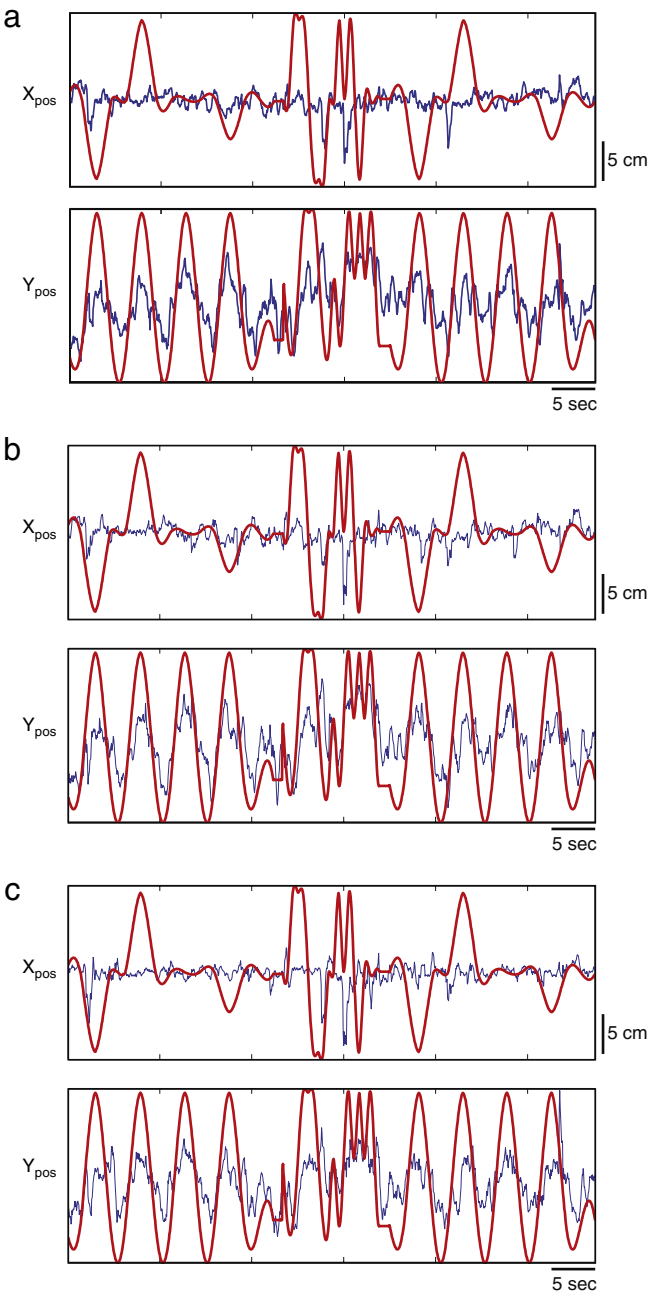

Fig. 6. Reconstructed trajectories from Wiener filters for Patient 2 (in blue) projected on the cursor trajectories (in red) with (a) $n = 32$, (b) $n = 16$, (c) $n = 8$ bands. (For interpretation of the references to colour in this figure legend, the reader is referred to the web version of this article.)

behavior and extraneous activity, as well as acquisition noise. Therefore, with linear modeling, reconstructed trajectories are restricted to be a combination of the motor control features and irrelevant activity riding on them. With nonlinear translations, the noise within ECoG BMI features and the motor control features can be projected into different areas of the output space.

Time delay neural networks (TDNNs), the most common neural architecture for dynamical modeling, have been used in BMI experiments (Kim, 2005) and offer a nonlinear mapping through hidden processing elements. However, the number of parameters of the model scales the high dimensional input and thus creates problems with model generalization. Moreover, the size of the training data required for good approximation increases with the number of parameters. To overcome the problem of model order, recurrent neural networks (RNNs) have been implemented in BMIs (Sanchez et al., submitted for publication) as they employ only current data samples and defer the memory structure to the hidden, recurrent layer instead of time-embedding. Various algorithms, such as backpropagation through time and real-time recurrent learning (Williams & Zipser, 1989), have been proposed to train RNNs; however, these algorithms suffer from computational complexity, resulting in slow training and possibly instability (Haykin, 1998). For real-time clinical applications, models of low order that are easy to train with low memory requirements are desirable.

3.2.1. Echo state networks

For BMIs, the best compromise of training, computational complexity, nonlinearity, and dynamics can be achieved by

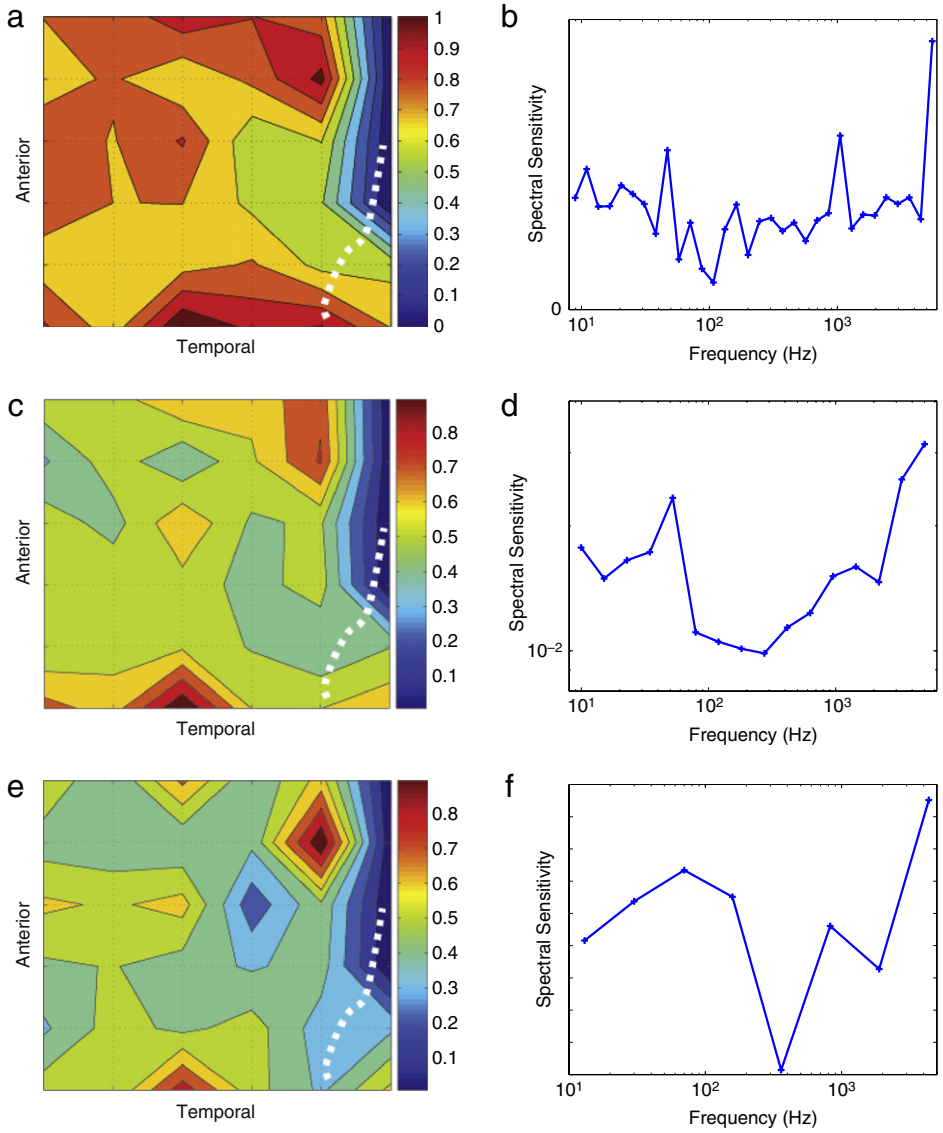

Fig. 7. Spatial and spectral sensitivities of Patient 1 with $L = 8$ order Wiener filters. (a) Spatial contribution of 32 channels across $n = 32$ passbands, (b) Spectral sensitivities of $n = 32$ passbands across the electrode grid. (c)–(d) Sensitivities for $n = 16$ passbands. (e)–(f) Sensitivities for $n = 8$ passbands. The central sulcus is shown on the grids with the white dotted line.

echo state networks (ESNs). ESNs are recurrent network (RNN) paradigms which address the difficulties with RNN training (Ozturk, Xu, & Principe, 2007). ESNs possess a large recurrent topology of nonlinear processing elements (PEs) which constitutes a "reservoir of rich dynamics" (Jaeger & Haas, 2004) and contain information about the history of input and output patterns when properly dimensioned (Jaeger, 2001). The outputs of these internal PEs (the echo states) are fed to a memoryless but adaptive readout network, which is generally linear, to produce the network output. The advantageous property of ESN is that only the linear memoryless readout is trained with a Wiener filter, whereas the recurrent topology $\mathbf{W}$ has fixed connection weights. This reduces the training complexity to simple linear regression while preserving the recurrent topology. Moreover, by integrating leaky neurons in the ESN structure, the memory depth of the system is increased without increasing filter orders (Gunduz et al., 2007).

Fig. 9 depicts an ESN with M input channels, N internal PEs and $C = 2$ output units. The input units, internal PEs, and output units at time n are donated by $\mathbf{u}(n) = \begin{bmatrix} u_1(n) & u_2(n) & \cdots & u_M(n) \end{bmatrix}$, $\mathbf{x}(n) = \begin{bmatrix} x_1(n) & x_2(n) & \cdots & x_N(n) \end{bmatrix}$, and $\mathbf{y}(n) = \begin{bmatrix} y_X(n) & y_Y(n) \end{bmatrix}$, respectively. The weights are given by an $N \times M$ matrix $\mathbf{W}^{\text{in}} = (w_{ij}^{\text{in}})$ for connections between the input and the states, by an $N \times N$ matrix $\mathbf{W} = (w_{ij})$ for connections between the PEs, by an $L \times N$ matrix $\mathbf{W}^{\text{out}} = (w_{ij}^{\text{out}})$ for connections from PEs to the output units, by an $N \times L$ matrix $\mathbf{W}^{\text{back}} = (w_{ij}^{\text{back}})$ for the connections that project back from the output to the internal PEs, by an $L \times M$ matrix $\mathbf{W}^{\text{inout}}$ for connections from input units to output units, and by an $L \times L$ matrix $\mathbf{W}^{\text{outout}}$ for connections between output units (Jaeger, 2001). The activation of the internal PEs is updated according to:

$$\mathbf{x}(n) = \boldsymbol{f}(\mathbf{W}^{in}\mathbf{u}(n) + \mathbf{W}\mathbf{x}(n-1) + \mathbf{W}^{\text{back}}\mathbf{y}(n-1)) \tag{11}$$

where $\boldsymbol{f} = (f_1, f_2, \ldots, f_N)$ are the internal unit's activation functions.

Alternatively, each PE can be implemented with a leaky integrator neuron with leakage parameter μ, decay rate α and the following update equation:

$$\mathbf{x}(n) = (1 - \mu\alpha)\mathbf{x}(n) + \mu\boldsymbol{f}(\mathbf{W}^{in}\mathbf{u}(n) + \mathbf{W}\mathbf{x}(n-1) + \mathbf{W}^{\text{back}}\mathbf{y}_C(n-1)). \tag{12}$$

The leaky neuron implementation utilizes the gamma delay operator in the recurrencies and is particularly useful when larger memory depths are required. Herein, for the sake of simplicity $\mathbf{W}^{\text{back}}$ is

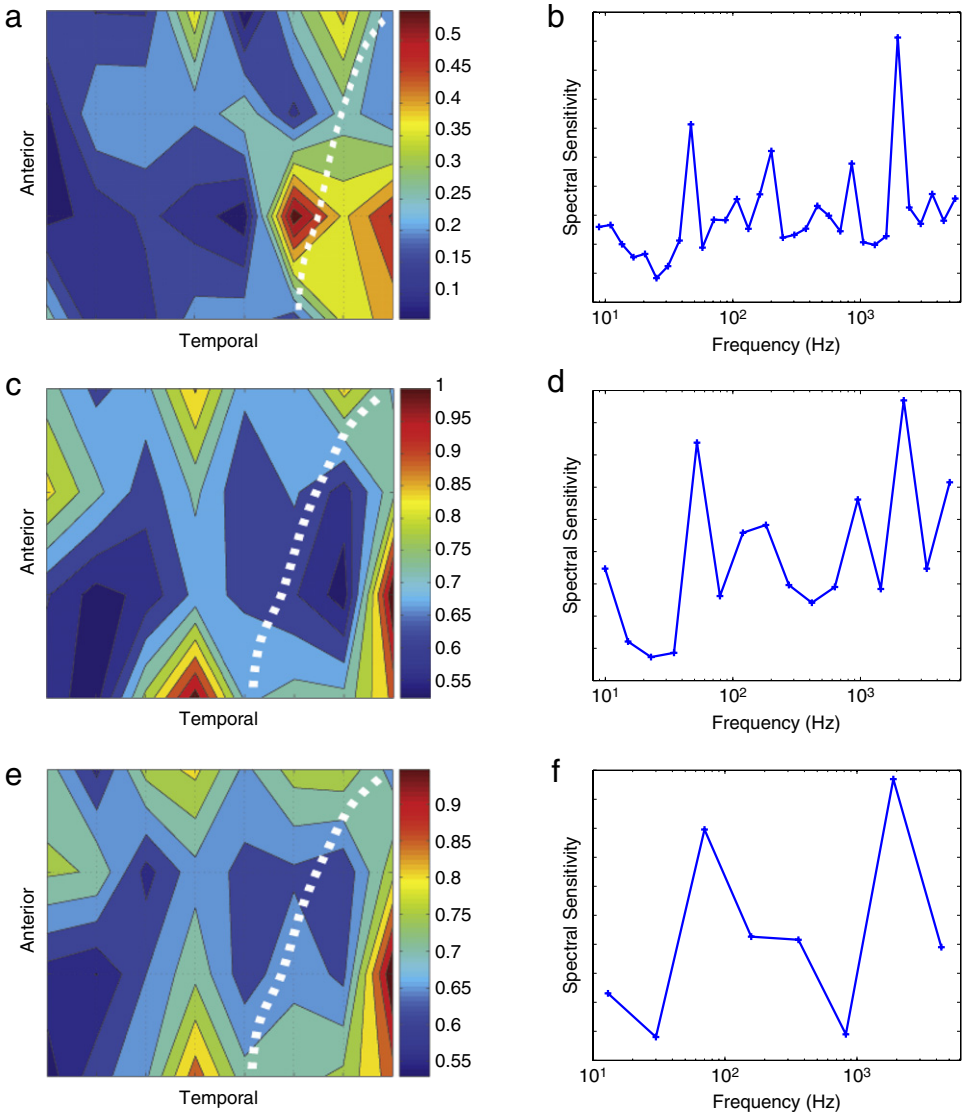

Fig. 8. Spatial and spectral sensitivities of Patient 2 with $L = 8$ order Wiener filters. (a) Spatial contribution of 32 channels across $n = 32$ passbands, (b) Spectral sensitivities of $n = 32$ passbands across the electrode grid. (c)–(d) Sensitivities for $n = 16$ passbands. (e)–(f) Sensitivities for $n = 8$ passbands. The central sulcus is shown on the grids with the white dotted line.

set to zero for both architectures. The output from the readout network is computed according to:

$$\mathbf{y}_C(n) = \boldsymbol{f}^{\text{out}}(\mathbf{W}_C^{\text{out}}\mathbf{x}(n) + \mathbf{W}^{\text{inout}}\mathbf{u}(n) + \mathbf{W}^{\text{outout}}\mathbf{y}(n-1)) \qquad (13)$$

where $\boldsymbol{f}^{\text{out}} = (f_1^{\text{out}}, f_2^{\text{out}}, \ldots, f_N^{\text{out}})$ are the output unit's nonlinear functions. Generally, the feedback loops from output-to-output and output-to-input are not connected and the readout is chosen to be linear (i.e. $\boldsymbol{f}^{\text{out}}$ is identity), in which case the optimal output weight matrix, $\mathbf{W}_C^{\text{out}}$, can computed using the Wiener solution.

Two basic reservoir properties have to be satisfied: the *input forgetting* and *state forgetting* properties which state that the reservoir must asymptotically forget the input history and the initial state, respectively. It has been shown in Jaeger (2001) that these two conditions are equivalent and both can be satisfied through the *echo state condition* of the spectral radius[4] of the reservoir weight matrix being less than unity, i.e. $\|\mathbf{W}\| < 1$. This condition states that the dynamics of the ESN is uniquely controlled by the recent input values and the effect of initial states vanishes. For the leaky neuron case, it is required that $\|\mu\mathbf{W} + (1 - \mu\alpha)\mathbf{W}\|$ be less than unity (Jaeger & Haas, 2004).

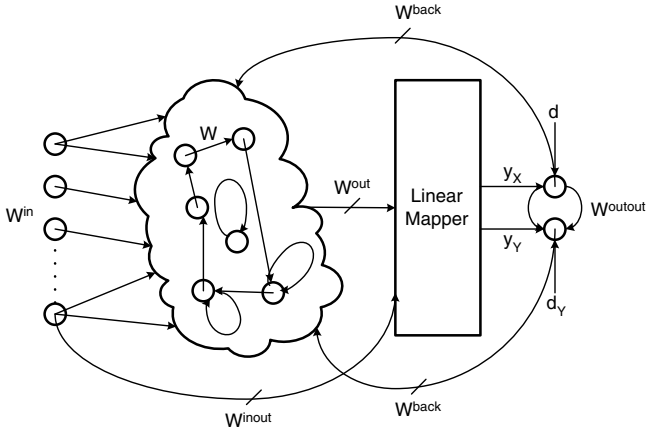

Fig. 9. Block diagram of an Echo state network.

[4] The spectral radius of a matrix is the largest magnitude of its eigenvalues.

Table 5
ESN performance results for Patient 1.

n	N	μ	$\|\mathbf{W}\|$	c	r_X	r_Y	MSE_X	MSE_Y
32	500	0.4	0.9	0.01	0.33 ± 0.25	0.85 ± 0.17	0.98 ± 0.54	0.27 ± 0.16
	2500	0.3	0.9	0.01	0.43 ± 0.30	0.85 ± 0.13	0.92 ± 0.57	0.57 ± 0.29
16	500	0.3	0.9	0.01	0.54 ± 0.28	0.82 ± 0.21	0.90 ± 0.43	0.43 ± 0.36
	2500	0.3	0.9	0.01	0.53 ± 0.22	0.83 ± 0.19	0.84 ± 0.39	0.28 ± 0.18
8	**500**	0.2	0.9	0.1	$\mathbf{0.51} \pm 0.26$	$\mathbf{0.85} \pm 0.18$	0.95 ± 0.55	0.30 ± 0.16
	1000	0.8	0.9	0.01	0.39 ± 0.29	0.85 ± 0.14	0.99 ± 0.59	0.31 ± 0.16

Table 6
ESN performance results for Patient 2.

n	N	μ	$\|\mathbf{W}\|$	c	r_X	r_Y	MSE_X	MSE_Y
32	250	0.2	0.9	0.01	0.41 ± 0.28	0.74 ± 0.22	1.19 ± 1.36	0.48 ± 0.27
	1000	0.2	0.9	0.01	0.41 ± 0.25	0.71 ± 0.21	1.20 ± 1.30	0.48 ± 0.26
16	1000	0.1	0.9	0.1	0.44 ± 0.28	0.75 ± 0.26	1.22 ± 1.37	0.43 ± 0.24
	2000	0.1	0.9	0.01	0.56 ± 0.24	0.81 ± 0.24	1.12 ± 1.42	0.46 ± 0.18
8	**500**	0.1	0.9	0.1	$\mathbf{0.61} \pm 0.28$	$\mathbf{0.80} \pm 0.25$	1.16 ± 1.40	$\mathbf{0.35} \pm 0.23$
	1000	0.1	0.9	0.1	0.55 ± 0.28	0.76 ± 0.28	0.99 ± 1.17	0.38 ± 0.22

In addition to the echo state conditions on the reservoir matrix, Ozturk et al. (2007) proposed uniform reservoir pole distributions covering the frequency spectrum optimally. Uniformly distributed poles within the unit circle provide uniform coverage of time constants of the underlying system as uniformly distributed phases create filters with different center frequencies and inner versus poles closer to the unit circle provide large frequency support versus narrow bandpass filters (Ozturk et al., 2007). Uniformly distributed poles within the unit circle can be attained by iteratively maximizing the entropy of the distribution of randomly initialized all-pole filters as described in Erdogmus, Hild, and Principe (2003). The reservoir matrix, $\mathbf{W}$ can then be designed based on the coefficients of the characteristic polynomial with the direct canonical structure that guarantees sparseness (Ozturk et al., 2007):

$$\mathbf{W} = \begin{bmatrix} -a_1 & -a_2 & \cdots & -a_{N-1} & -a_N \\ 1 & 0 & \cdots & 0 & 0 \\ 0 & 1 & \cdots & 0 & 0 \\ \cdots & \cdots & \cdots & \cdots & \cdots \\ 0 & 0 & \cdots & 1 & 0 \end{bmatrix} \tag{14}$$

where the coefficients of the characteristic polynomial, a_i, are attained from the uniformly distributed poles, i.e. the eigenvalues of the reservoir matrix.

3.2.2. Echo state networks for ECoG BMIs

For the application of ESNs to our BMI problem, we first initialize the input matrix $\mathbf{W}^{\text{in}}$ with uniformly distributed random numbers scaled between $[-0.05, 0.05]$. These boundary values are chosen such that for the largest spectral radius, $r = 0.9$, the states are not overly saturated. The nonlinearity in the reservoir is chosen to be the hyperbolic tangent function, $f(x) = \tanh(x)$. The parameters that are varied are the number of echo states, $N = \{250, 500, 1000, 2000, 2500\}$, the reservoir spectral radius, $r = \{0.5, 0.7, 0.9\}$ and the leakage parameter $\mu = \{0.1, 0.2, \ldots, 1.0\}$ (where $\mu = 1$ corresponds to the regular/non-leaky ESN).

Due to the large number of states and the minor deviations from uniform distribution due to details of entropy estimation (Erdogmus et al., 2003), reservoir matrices formed of elements that take on the values $\{0, -1, 1\}$ with probabilities $p, (1-p)/2, (1-p)/2$ respectively, provide similar close-to-uniform pole distributions within the unit circle when $\mathbf{W}$ is normalized by its the maximum eigenvalue and scaled by the desired spectral radius. The probability p represents the sparseness of the reservoir matrix. For the experiments herein, we set $p = 0.95$.

The first second of the states is discarded as transient activity before attaining the least square solution for the output weights, $\mathbf{W}_C^{\text{out}}$. Due to random initializations of the input and reservoir matrices, fifteen Monte Carlo simulations were run for each set of parameters. The ESNs are trained on the same training sets as the linear filters. Performance results from selected simulations for both patients are presented in Tables 5 and 6, respectively.

Overall, the leaky ESN, which adds memory depths to the model, yielded better performance than the regular ESN architecture. The spectral radius of 0.9, which provides the highest variance in the states, also provided better performance across all parameters and both patients. As in the case of linear models, the vertical trajectory reconstruction performance is far better that the horizontal case. Exemplary trajectories of the reconstructed trajectories are depicted in Figs. 10 and 11.

3.2.3. Sensitivity analysis

Comparing the spectral and spatial sensitivities of linear and nonlinear models can provide insight to the differences in the projection space formed by each model. For the nonlinear models, we study the rate of changes in the model outputs as the modulation of channels varies over time. Due to the hidden layer, we apply the chain rule to form this relationship:

$$\frac{\partial \mathbf{y}(n)}{\partial \mathbf{u}(n)} = \frac{\partial \mathbf{y}(n)}{\partial \mathbf{x}(n)} \frac{\partial \mathbf{x}(n)}{\partial \mathbf{u}(n)} = (\mathbf{W}_C^{\text{out}})^T \mathbf{D}_n \mathbf{W}^{\text{in}} \tag{15}$$

$$\frac{\partial \mathbf{y}(n)}{\partial \mathbf{u}(n-1)} = (\mathbf{W}_C^{\text{out}})^T \mathbf{D}_n \mathbf{W}^T \mathbf{D}_{n-1} \mathbf{W}^{\text{in}} \tag{16}$$

$$\frac{\partial \mathbf{y}(n)}{\partial \mathbf{u}(n-\Delta n)} = (\mathbf{W}_C^{\text{out}})^T \mathbf{D}_n \left(\prod_{i=1}^{\Delta n} \mathbf{W}^T \mathbf{D}_{n-i} \right) \mathbf{W}^{\text{in}} \tag{17}$$

where $\mathbf{D}_n = \text{diag}\left[\boldsymbol{f}'(z_1(n))\boldsymbol{f}'(z_2(n))\cdots\boldsymbol{f}'(z_N(n))\right]$ and $\mathbf{z}(n) = \mathbf{W}^{\text{in}}\mathbf{u}(n) + \mathbf{W}\mathbf{x}(n-1)$. This yields an instantaneous sensitivity of the output to one of the inputs. The temporal decay of inputs is plotted in Fig. 12. Experimentally, we determine the sensitivity depth to be around 2 s. Hence at each time stamp the temporal sensitivity of the output to an input is computed as the averages of the instantaneous sensitivities over 3 s (an additional second guarantees decayed sensitivities). We further average across passbands and channels to attain the spatial and spectral sensitivities of the recurrent network. These measures are presented in Figs. 13 and 14. For Patient 1, the spatial sensitivity of the $n = 32$ bands is widespread with high localizations in the PMd and M1 areas. Just like in the Wiener filter case, with

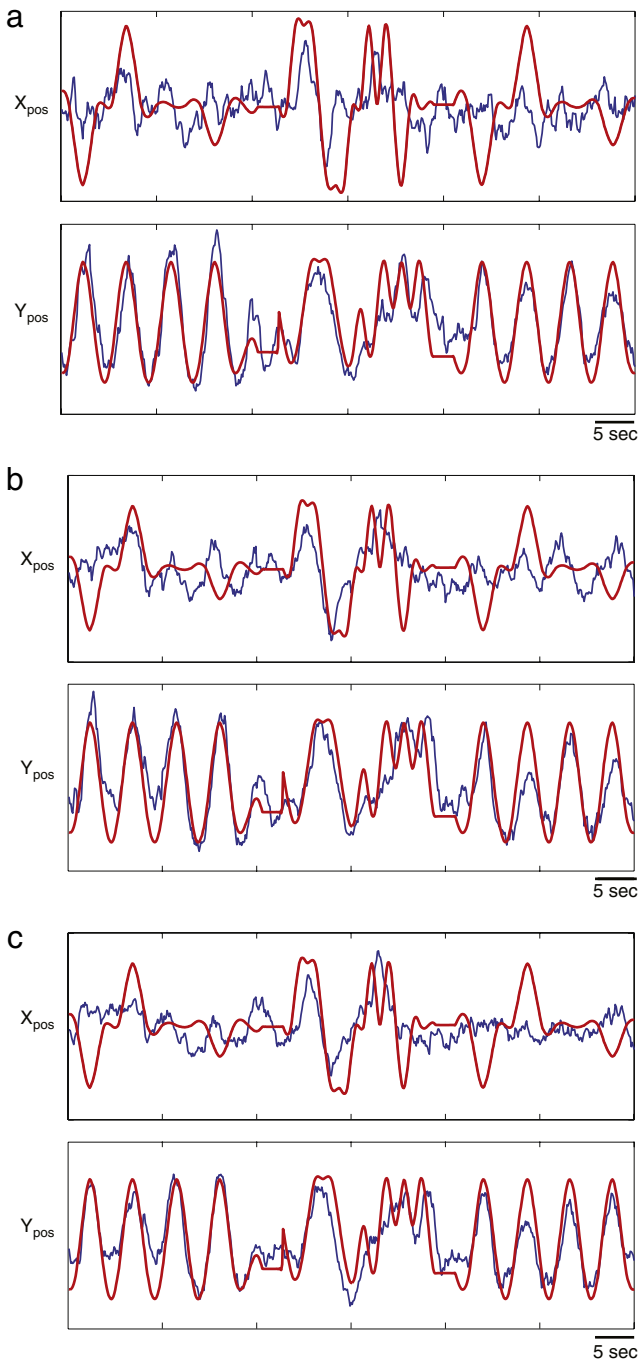

Fig. 10. Reconstructed trajectories from Wiener filters for Patient 1 (in blue) projected on the cursor trajectories (in red) with (a) $n = 32$, (b) $n = 16$, (c) $n = 8$ bands with $N = 500$ states. (For interpretation of the references to colour in this figure legend, the reader is referred to the web version of this article.)

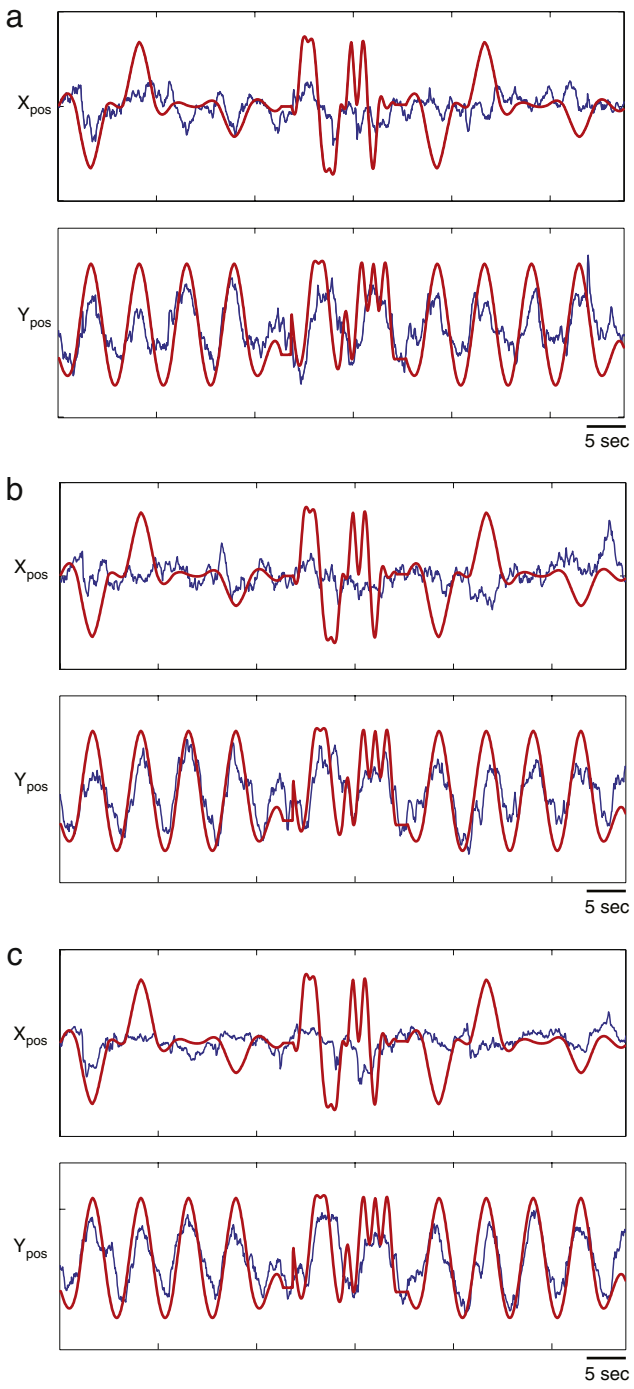

Fig. 11. Reconstructed trajectories from ESNs for Patient 2 (in blue) projected on the cursor trajectories (in red) with (a) $n = 32$, (b) $n = 16$, (c) $n = 8$ bands with $N = 1000$ states. (For interpretation of the references to colour in this figure legend, the reader is referred to the web version of this article.)

a lower number of bands, we have narrower spatial sensitivities. Moreover, the spatial sensitivities of the ESNs and Wiener filter overlap. In the case of spectral sensitivities, ESNs and the Wiener filters identify the same spectral ranges as the most sensitive. Similar observations can be made with Patient 2. Spatial sensitivity is widespread in the case $n = 32$ with high positive and negative sensitivities overlapping with those of the Wiener filter. Areas with high spatial sensitivities become narrower with $n = 16, 8$ bands. Finally, the same sensitive spectral ranges as the Wiener filter are captured.

4. Discussion

In this study we showed the feasibility of reconstructing of two-dimensional hand trajectories with high resolution broadband ECoG via linear and nonlinear models with embedded memory depths. Three avenues for are explored for maximal decoding performance. First, we varied how finely we divided the ECoG spectrum. Second, we vary how much memory, or time embedding, is employed by the decoding models. Third, we provided a comparison on linear and nonlinear decoding models. Overall, this pa-

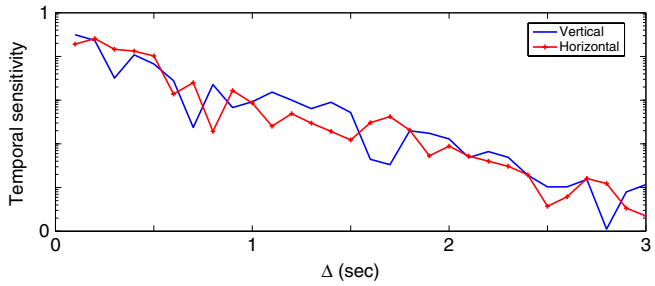

Fig. 12. Sensitivity at time t for channel 1 of Patient 1 with $n = 32$ bands as a function of Δ.

per presents a systematic analysis of the bounds on the required complexity of ECoG decoders and provides much needed studies on ECoG spectral range, spectral decomposition and nonlinear BMI projections.

The following subsections summarize our findings, mainly the spectral and spatial contributions and present comparison of reconstruction performance across trajectory axes and patients, as well as an insight to how the significance of the results were verified.

4.1. Spectral resolution of broadband ECoG features

Spectral sensitivity analyses demonstrate the presence of motor control features in ECoG up to 6 kHz in Fig. 7(d)–(f). Hence, ECoG signal acquisition systems should utilize higher sampling rates than those clinically used for EEG. Extracting features in this vast input space, however, has to be systematically facilitated, which arises the question of resolution in the spectral decomposition. We reconstructed trajectories from features at three different levels of spectral resolution. As there were no significant differences in performance, we can conclude that the lowest resolution level at which the well-known neurophysiological rhythms are maintained ($n = 8$) is the optimal resolution as it minimizes the number of parameters involved in the models. Furthermore, well known neural rhythms over the motor cortex (such as mu, beta, gamma, fast gamma) are captured within one passband with $n = 8$ bands which were otherwise split with higher resolution. This supports

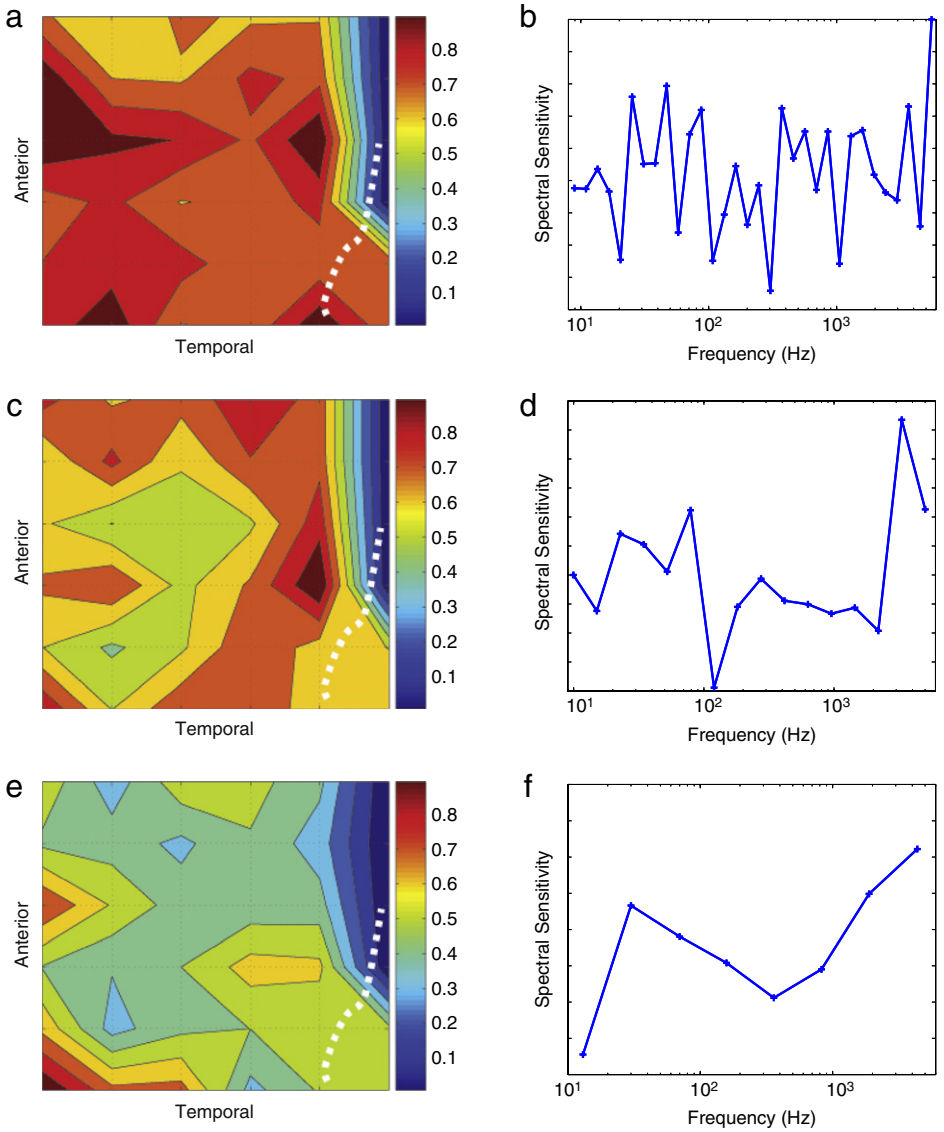

Fig. 13. Spatial and spectral sensitivities of ESNs with $N = 500$ states for Patient 1. (a) Spatial contribution of 32 channels across $n = 32$ passbands, (b) Spectral sensitivities of $n = 32$ passbands across the electrode grid. (c)–(d) Sensitivities for $n = 16$ passbands. (e)–(f) Sensitivities for $n = 8$ passbands. The central sulcus is shown on the grids with the white dotted line.

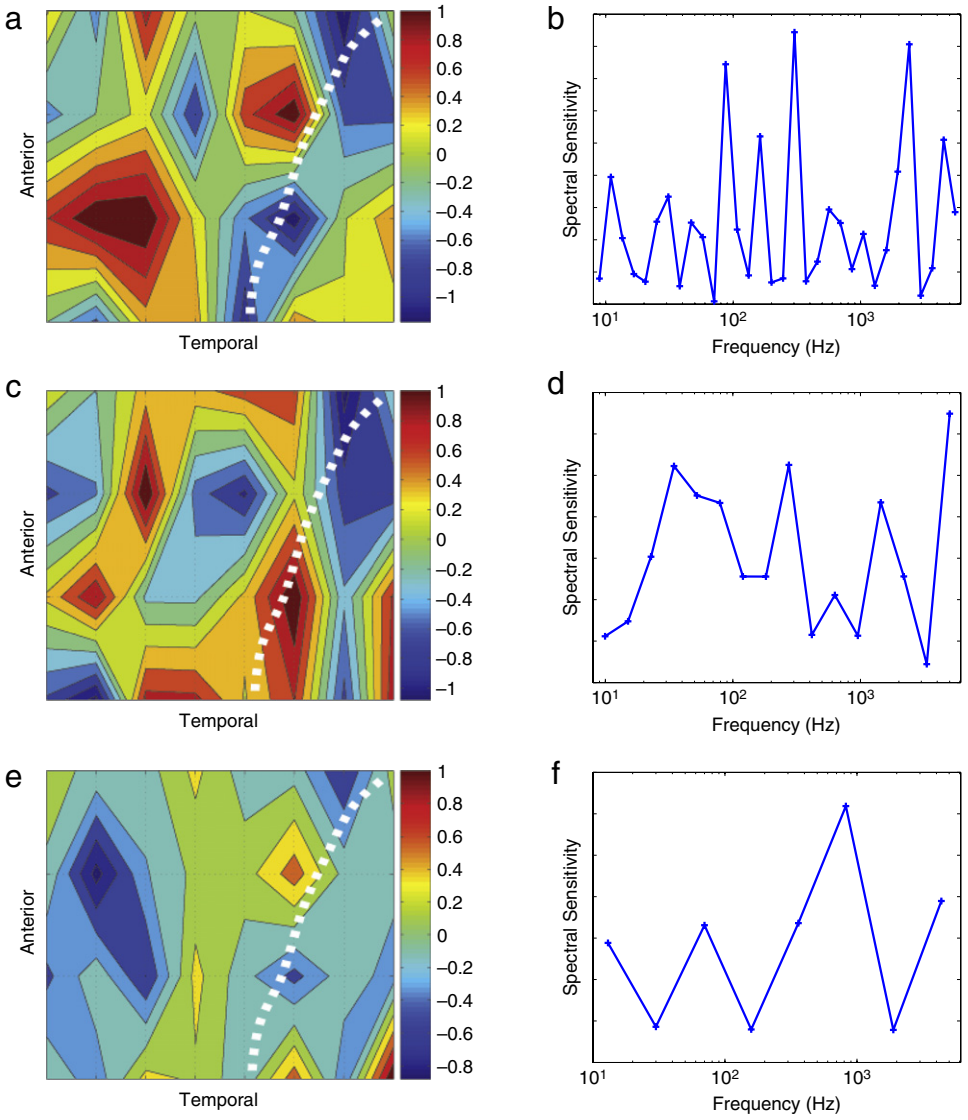

Fig. 14. Spatial and spectral sensitivities of ESNs with $N = 1000$ states for Patient 2. (a) Spatial contribution of 32 channels across $n = 32$ passbands, (b) Spectral sensitivities of $n = 32$ passbands across the electrode grid. (c)–(d) Sensitivities for $n = 16$ passbands. (e)–(f) Sensitivities for $n = 8$ passbands. The central sulcus is shown on the grids with the white dotted line.

the empirical finding that $n = 8$ Q-bands yield the optimal spectral resolution for the decomposition of the broadband spectrum between 8 Hz–6 kHz. Further merging these bands, leads to deteriorated reconstruction performances as previously reported in Sanchez et al. (2008).

Again from Fig. 7(d)–(f), we observe that when the number of spectral bands were reduced from 32 to 16 and then to 8, contributions from some of the passbands are lost. However, these losses are compensated by putting more emphasis on the important spatiotemporal features that were preserved. This can explain the narrower spatial sensitivity localizations in Fig. 7(a)–(c). Similar observations are made with the nonlinear spectral sensitivities, with fewer bands, we have narrower spatial sensitivities (see Fig. 13).

4.2. Spatial contributions of broadband ECoG

The most sensitive channels identified with linear sensitivity analysis not only capture the electrodes over the responsive electrodes, but they are also in accord with those found to be highly correlated to behavior, extracted through source separation and that are directionally tuned to trajectories in Gunduz et al. (in preparation). For Patient 1, the nonlinear spatial sensitivity of the $n = 32$ bands is widespread with high localizations in the PMd and M1 areas. Moreover, the spatial sensitivities of ESNs and Wiener filter overlap (Figs. 7 and 13). Similar observations can be made with Patient 2. Spatial sensitivity is widespread in the case $n = 32$ with high positive and negative sensitivities overlapping with those of the Wiener filter (8 and 14). However, we must note that the nonlinear sensitivities are initialization dependent and slightly alter from one simulation to the other.

4.3. Nonlinear mapping through ESNs

For Patient 1, the nonlinear recurrent architecture has not provided a statistically significance over the linear methods. This may be due to the fact that it was possible to find a projection to the low dimensional trajectories from the very high dimensional input space. However, in a previous study (Gunduz et al., 2007) in which we had coarsely divided the broadband spectrum into four bands between: 1–60 Hz, 60–100 Hz, 100–300 Hz and 300 Hz–6 kHz, the ESNs were able to identify the sensitive portions of the highest

Table 7
Performance comparison of linear and non-linear filters for Patient 1 with $n = 4$ spectral bands.

Frequency bands	Wiener filter		ESN		Leaky ESN	
	r_X	r_Y	r_X	r_Y	r_X	r_Y
300–6 kHz	0.39 ± 0.26	$\mathbf{0.48} \pm 0.27$	0.50 ± 0.27	$\mathbf{0.61} \pm 0.29$	0.49 ± 0.26	$\mathbf{0.63} \pm 0.28$
100–300 Hz	0.34 ± 0.21	0.35 ± 0.25	0.33 ± 0.22	0.50 ± 0.27	0.36 ± 0.26	0.52 ± 0.27
60–100 Hz	0.35 ± 0.24	0.41 ± 0.22	0.37 ± 0.25	0.39 ± 0.23	0.43 ± 0.25	0.45 ± 0.26
1–60 Hz	0.33 ± 0.16	0.41 ± 0.25	0.39 ± 0.26	0.43 ± 0.26	0.41 ± 0.25	0.44 ± 0.26

frequency band and yielded statistically significant reconstruction performance (refer to Table 7). In other words, ESNs were able to prune the features that contributed to the reconstruction of the trajectories in a coarse spectral resolution much better than the linear filters. As the performance of the linear models and ESNs is statistically equivalent for both the maximal resolution of $n = 32$ and minimal resolution of $n = 8$ in our current study, we conclude that the higher bands do not require further splitting. The equivalence of performance in the current study can be attributed to the fine spectral resolution of the current feature sets.

On the other hand, for Patient 2, t-tests reveal an improvement in the MSE values of the vertical reconstruction over the linear filters at a significance level of 0.05, for all three choices of number of spectral bands. This result may be a reflection of the interictal activity in Patient 2. The interictal activity in Patient 1 consists of quasi-periodic spikes (see Gunduz, Sanchez, and Principe (2008) and the linear filters may have been able to compensate for such artifacts. On the other, the interictal artifacts observed with Patient 2 are spontaneous bursty activities. The nonlinear filters may have been able to mitigate the effects of this sort of artifact. Overall, we can conclude that nonlinear models perform better in the undesired cases of low spectral resolution and abundance of random interictal activity.

4.4. Reconstruction from a vast feature space

Despite the vast amount of extracted features, the designed linear and nonlinear filters were able to capture the features that had proved to be highly correlated with behavior through the earlier analyses (Gunduz et al., in preparation). Due to the dynamic, nonstationary nature of neural modulations, these results are in fact encouraging because in a closed-loop system users may be able to modulate a band with more ease over another, or the sensitive spectral bands may change from session to session, or the spatial sensitivity might change from task to task. Therefore, instead of performing subspace projection or feature selection, having the luxury of feeding every band and every channel would prove useful in practice.

4.5. Comparison of reconstruction across dimensions and subjects

We cannot ignore mentioning the performance difference between the vertical and horizontal axes of the trajectory in all models. In Gunduz et al. (in preparation), we show through crosscorrelation analysis that the horizontal trajectory is less correlated with the ECoG activity for both patients. This may be related to the low deviation of motion from the origin in the horizontal direction. Especially in the target selection task, the span of the vertical axis is much larger. Such differences in performance across two dimensions were also reported by Schalk et al. (2007). In future studies, experiments will be designed to allow for equal variance and symmetric stretch in both dimensions.

It is also possible that the coverage of the electrodes capturing neural representation is better in one direction of movement than the other. As listed in Table 1, Patient 1 responded to more electrodes with more muscles sets in the right arm when electrically stimulated, compared to Patient 2. Also, in Gunduz et al. (2008) we show that the interictal activity in Patient 1 is quasiperiodic and more localized which may be overcome through linear filters, whereas the interictal activity of Patient 2 is bursty and spread across the whole electrode grid, affecting the reconstruction performance. In either case, the results of this study several of the challenges in ECoG BMI modeling and provides a methodology to appropriately select ECoG neural input features and model topologies to contend with clinical neuroprosthetic signals.

4.6. Verification of contribution from high spectral features

Verification of the contribution of the high spectral features (300 Hz–6 kHz) to the performance is important as these findings were not reported in previous literature and due to concerns of signal-to-noise ratios at such high frequencies.[5] First, an event-related spectral analysis was performed by comparing the spectra during movement and at rest conditions. An increase in power in the high frequency bands that were found to be important in the sensitivity analyses was observed during task execution versus the rest state (for plots see Gunduz et al. (in preparation)). Second, surrogate datasets were created by randomizing the phase of the raw ECoG recordings while preserving the Fourier amplitudes and hence the spectra (Prichard & Theiler, 1994). If similar performance results were to be found with the surrogates, then the results would be superficial and attributable to chance. However, as was reported in our previous studies (Sanchez et al., 2008), the performance results suffer immensely with the surrogate data. When the power of both the original and surrogate data highpass filtered above 300 Hz are fed into the Wiener filter, the respective Pearson's r values were 0.48 ± 0.27 and 0.09 ± 0.29 for vertical trajectory reconstruction. This shows that in fact the reconstruction performance of the high power components are well above the chance levels attained with the surrogates.[6]

Acknowledgments

The authors would like to thank the reviewers for their invaluable comments and suggestions which have been incorporated into this manuscript, as well as Andrew Hoyord from Tucker–Davis Technologies for conducting the noise floor measurements.

References

Carmena, J. M., Lebedev, M. A., Crist, R. E., O'Doherty, J. E., Santucci, D. M., Dimitrov, D. F., et al. (2003). Learning to control a brain–machine interface for reaching and grasping by primates. *PLoS Biology*, *1*(2).

Chin, C. M., Popovic, M. R., Thrasher, A., Cameron, T., Lozano, A., & Chen, R. (2007). Identification of arm movements using correlation of electrocorticographic spectral components and kinematic recordings. *Journal of Neural Engineering*, *4*(2), 146+.

Desmurget, M., Pelisson, D., Rossetti, Y., & Prablanc, C. (1998). From eye to hand: Planning goal-directed movements. *Neuroscience & Biobehavioral Reviews*, *22*, 761.

[5] The bioamplifiers employed in this study were TDT Medusa preamplifiers which have an 6 μV rms and $8n$ V/$\sqrt{\text{Hz}}$.

[6] A final verification was done through the denoising source separation methodology (Sarela & Valpola, 2005) which is beyond the scope of this paper and explained in detail in Gunduz et al. (in preparation).

Donoghue, J. P., Nurmikko, A., Black, M., & Hochberg, L. R. (2007). Assistive technology and robotic control using motor cortex ensemble-based neural interface systems in humans with tetraplegia. *The Journal of Physiology*, *579*(3), 603–611.

Erdogmus, D., Hild, K., & Principe, J. (2003). Online entropy manipulation: Stochastic information gradient. *IEEE Signal Processing Letters*, *10*, 242–245.

Felton, E. A., Wilson, J. A., Williams, J. C., & Garell, P. C. (2007). Electrocorticographically controlled brain–computer interfaces using motor and sensory imagery in patients with temporary subdural electrode implants. *Journal of Neurosurgery*, *106*, 495–500.

Freeman, W. (2006). Definitions of state variables and state space for brain computer interfaces. *Cognitive Neuroscience*, *1*, 3–14.

Georgopoulus, A. P., Kalaska, J. F., Caminiti, R., & Massey, J. T. (1982). On the relations between direction of two-dimensional hand movements and cell discharge in primate motor cortex. *Journal of Neuroscience*, *2*, 1527–1537.

Gunduz, A., Ozturk, M., Sanchez, J., & Principe, J. (2007). Echo state networks for motor control of human ecog neuroprosthetics. In *Proceedings of IEEE conference on neural engineering*.

Gunduz, A., Sanchez, J., Carney, P., & Principe, J. (2009). Analysis of movement-related features in broadband human electrocorticography for deciphering two-dimensional hand trajectories. (in preparation).

Gunduz, A., Sanchez, J., & Principe, J. (2008). Electrocorticographic interictal spike removal via denoising source separation for improved neuroprosthesis control. In *IEEE engineering in medicine and biology conference proceedings*.

Haykin, S. (1998). *Neural networks: A comprehensive foundation* (2nd ed.). Prentice Hall.

Haykin, S. (2001). *Adaptive filter theory* (4th ed.). Prentice Hall.

Hochberg, L. R., Serruya, M. D., Friehs, G. M., Mukand, J. A., Saleh, M., Caplan, A. H., et al. (2006). Neuronal ensemble control of prosthetic devices by a human with tetraplegia. *Nature*, *442*(7099), 164–171.

Jaeger, H. (2001). The "echo state" approach to analyzing and training recurrent neural networks. *GMD report 148*. GMD-German National Research Institute for Computer Science.

Jaeger, H., & Haas, H. (2004). Harnessing nonlinearity: Predicting chaotic systems and saving energy in wireless communication. *Science*, *304*(5667), 78–80.

Kennedy, P. R., Kirby, M. T., Moore, M. M., King, B., & Mallory, A. (2004). Computer control using human intracortical local field potentials. *IEEE Transactions on Neural Systems and Rehabilitation Engineering*, *12*, 339–344.

Kim, S.-P. (2005). Design and analysis of optimal decoding models for brain–machine interfaces. *Ph.d. thesis*. University of Florida.

Kim, S.-P., Sanchez, J. C., Rao, Y. N., Erdogmus, D., Principe, J. C., Carmena, J. M., et al. (2006). A comparison of optimal mimo linear and nonlinear models for brain–machine interfaces. *Journal of Neural Engineering*, *3*, 145–161.

Leuthardt, E., Schalk, G., Wolpaw, J., Ojemann, J., & Moran, D. (2004). A brain-computer interface using electrocorticographic signals in humans. *Journal of Neural Engineering*, *1*(2), 63–71.

Leuthardt, E. C., Schalk, G., Moran, D., & Ojemann, J. G. (2006). The emerging world of motor neuroprosthetics: A neurosurgical perspective. *Neurosurgery*, *59*(1), 1–14.

Mehring, C., Nawrot, M. P., de Oliveira, S. C., Vaadia, E., Schulze-Bonhage, A., Aertsen, A., et al. (2004). Comparing information about arm movement direction in single channels of local and epicortical field potentials from monkey and human motor cortex. *Journal of Physiology-Paris*, *98*(4-6), 498–506.

Nunez, P. L., & Srinivasan, R. (2005). *Electric fields of the brain: The neurophysics of EEG*. Oxford University Press.

Ozturk, M., Xu, D., & Principe, J. (2007). Analysis and design of echo state networks for function approximation. *Neural Computation*, *19*.

Pistohl, T., Ball, T., Schulze-Bonhage, A., Aertsen, A., & Mehring, C. (2008). Prediction of arm movement trajectories from ecog-recordings in humans. *Journal of Neuroscience Methods*, *167*(1), 105–114.

Prichard, D., & Theiler, J. (1994). Generating surrogate data for time series with several simultaneously measured variables. *Physical Review Letters*, *73*, 951–954.

Principe, J. C., Vries, B. D., & Oliveira, P. G. D. (1993). The gamma filter—A new class of adaptive iir filters with restricted feedback. *IEEE Transactions on Signal Processing*, *41*, 649–656.

Rao, Y., Kim, S. -P., Sanchez, J., Erdogmus, D., Principe, J., & Carmena, J. et al. (2005). Learning mappings in brain machine interfaces with echo state networks. In *Proceedings of IEEE international conference on acoustics, speech, and signal processing*.

Sanchez, J., Carmena, J., Lebedev, M., Nicolelis, M., & Harris, J. P. (2003). Ascertaining the importance of neurons to develop better brain machine interfaces. *IEEE Transactions on Biomedical Engineering*, *61*, 943–953.

Sanchez, J., Erdogmus, D., Y. R., Hild, K., Wessberg, J., & Nicolelis, M. et al. (2005). Analysis of the neural to motor representation space constructed by a recurrent neural network trained for a brain–machine interface. *Neural Computation* (submitted for publication).

Sanchez, J., Gunduz, A., Carney, P., & Principe, J. (2008). Extraction and localization of mesoscopic motor control signals for human ecog neuroprosthetics. *Journal of Neuroscience Methods*, *167*(1), 63–81.

Sarela, J., & Valpola, H. (2005). Denoising source separation. *Journal of Machine Learning Research*, *6*, 233–272.

Schalk, G., Kubánek, J., Miller, K. J., Anderson, N. R., Leuthardt, E. C., Ojemann, J. G., et al. (2007). Decoding two-dimensional movement trajectories using electrocorticographic signals in humans. *Journal of Neural Engineering*, *4*(3), 264+.

Smaragdis, P. (2001). Redundancy reduction for computational audition, a unifying approach.*Ph.d. thesis*. Massachusetts Institute of Technology.

Uematsu, S., Lesser, R., Fisher, R., Gordon, B., Hara, K., Krauss, G., et al. (1992). Motor and sensory cortex in humans: Topography studied with chronic subdural stimulation. *Neurosurgery*, *31*, 59–72.

Wessberg, J., Stambaugh, C. R., Kralik, J. D., Beck, P. D., Laubach, M., Chapin, J. K., et al. (2000). Real-time prediction of hand trajectory by ensembles of cortical neurons in primates. *Nature*, *408*(6810), 361–365.

Williams, R. J., & Zipser, D. (1989). A learning algorithm for continually running fully recurrent neural networks. *Neural Computation*, *1*(2), 270–280.